

How different is the magnetic field at the core-crust interface from that at the neutron star surface?:the range allowed in magnetoelastic equilibrium

Yasufumi Kojima ^{*1}, Shijun Yoshida²

¹*Department of Physics Graduate School of Advanced Science and Engineering, Hiroshima University Higashi-Hiroshima 739-8526, Japan*

²*Astronomical Institute, Tohoku University, Sendai 980-8578, Japan*

19 October 2023

ABSTRACT

This study was focused on the investigation of a magnetic field penetrating from the core of a neutron star to its surface. The range of possible field configurations in the intermediate solid crust is less limited owing to the elastic force acting on the force balance. When the Lorentz force is excessively strong, the magnetoelastic equilibrium does not hold, and thus, the magnetic field becomes constrained. By numerically solving for the magnetoelastic equilibrium in a thin crust, the range of the magnetic field at the core–crust interface was determined, while assuming the exterior to be fixed as a dipole in vacuum. The results revealed that the toroidal component should be smaller than the poloidal component at the core–crust interface for the surface dipole, $B_0 > 2.1 \times 10^{14}$ G. Consequently, a strong toroidal field, for example, $B \sim 10^{16}$ G, as suggested by free precession of magnetars should be confined to a deep interior core and should be reduced to $B \sim 10^{14}$ G at the bottom of the crust. The findings of this study provide insights into the interior field structure of magnetars. Further investigations on more complicated geometries with higher multipoles and exterior magnetosphere are necessary.

Key words: stars: neutron stars; magnetars: magnetic fields.

1 INTRODUCTION

A neutron star is surrounded by a thin, light shell called the crust. Its thickness is less than 0.1 times the stellar radius, while its mass is less than 0.01 of the total mass (for example [Shapiro & Teukolsky 1983](#)). Therefore, the outer layer can be neglected in the first approximation when the entire stellar model is considered.

The ions in the crust constitute a Coulomb plasma, which is typically formed in crystals (for example [Chamel & Haensel 2008](#)). In contrast to fluids which are the primary material form in all stars, elastic media may be important for the crust-quake that occur in magnetars, which are strongly magnetized neutron stars ([Duncan & Thompson 1992](#); [Thompson & Duncan 1995](#), for a seminal paper). Sudden crust breaking can produce a magnetar outburst and/or a fast radioburst ([Lander et al. 2015](#); [Li et al. 2016](#); [Baiko & Chugunov 2018](#); [Suvorov & Kokkotas 2019](#)). The accumulation of shear stress toward crustal fractures owing to the evolution of the Hall magnetic field is studied ([Kojima 2022](#); [Kojima et al. 2023](#)). Recent theoretical works demonstrate that the elastic force plays a crucial role on the dynamical stability ([Bera et al. 2020](#)), and on static equilibrium models interiorly possessing strong magnetic field ([Kojima et al. 2021, 2022](#); [Fujisawa et al. 2022](#)).

The following question arises for a magnetic field penetrating from the inner core to the exterior vacuum: How much difference in magnitude is allowed between the magnetic field at the core–crust interface and that at the surface? This depends on the electric current distribution in the crust. However, determining the possible range is useful for further studies. Moreover, boundary conditions are imposed at the core–crust interface without detailed models in the crust when considering magnetic field in the core.

Free precessions of spinning magnetars observed in 4U 0142+63 ([Makishima et al. 2014, 2019](#)), in 1E 1547-54 ([Makishima et al. 2016, 2021a](#)), and in SGR 1900+14 ([Makishima et al. 2021b](#)) suggest a strong toroidal component relevant to deformation. The toroidal component inside these sources is $\sim 10^{16}$ G, whereas the surface dipole field is $(1.3 - 7) \times 10^{14}$ G. Such strong components may affect the magnetic structure of the crust unless it is confined to a deep interior. Our study provides useful information regarding magnetic field at the inner boundaries of the crust.

* E-mail: ykojima-phys@hiroshima-u.ac.jp

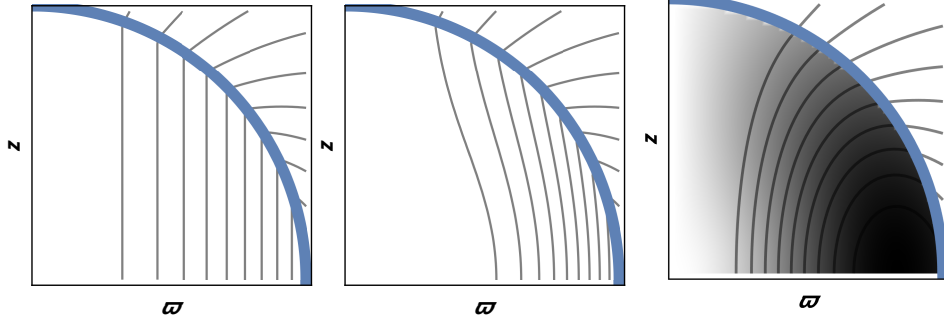


Figure 1. Three examples of magnetic fields penetrating the crust, denoted by the thick blue arc. Poloidal field lines and greyscale contour map of toroidal field B_ϕ are shown in meridian plane ($\varpi = r \sin \theta$, $z = r \cos \theta$). The left and middle panels exhibit $\Delta B_\theta \neq 0$ across the crust, while the right panel shows $\Delta B_\phi \neq 0$.

The permissible range depends on the configuration and strength of the magnetic field. The field configuration is arbitrary in the very weak case. As the field strength for the fixed configuration increases, the Lorentz force significantly affects force balance. We consider equilibrium with the Lorentz and elastic forces, because the latter in the crust is important for extending the range of the magnetic field configuration. However, the magnetoelastic force balance is disrupted when the elastic deformation exceeds a certain threshold. Thus, the constraint leads to an upper limit for the magnetic field strength.

We require the following minimum conditions for magnetic field geometry of the crust. The electric current in the thin layer is assumed to be described by a smooth function that matches the conditions on both sides of the spherical shell. This case is simple and natural for a thin crust. For a more complicated distribution, the magnetic field is tangled such that the contribution of the elastic force increased accordingly. Therefore, the constraints become more severe.

The remainder of this paper is organized as follows. The models and equations are discussed in Section 2. In Section 3, we calculate the magnetoelastic equilibrium for the minimum required electric currents and derive a change in the magnetic field across the crust. Finally, Section 4 concludes the study.

2 MATHEMATICAL FORMULATION

2.1 Magnetic field

We consider the magnetic field from the core–crust interface at r_c to surface at $R \equiv r_c + \Delta r$. The magnetic field was limited to an axially symmetric dipole, which is expressed in spherical coordinates (r, θ, ϕ) as follows:

$$B_r = \frac{2g}{r^2} \cos \theta, \quad B_\theta = -\frac{g'}{r} \sin \theta, \quad B_\phi = \frac{s}{r} \sin \theta, \quad (1)$$

where g and s are functions of r and prime $'$ denotes the derivative of r . In an external vacuum ($r \geq R$), these functions are expressed as

$$g = \frac{B_0 R^3}{2r}, \quad s = 0, \quad (2)$$

where B_0 is the field strength of the magnetic pole on the surface $r = R$.

When the thickness Δr is small $\Delta r \ll r_c$, the change in of the magnetic field along a fixed polar angle θ can be approximated as follows:

$$\Delta B_r \equiv B_r(R, \theta) - B_r(r_c, \theta) \equiv B_0 \Delta \alpha \cos \theta, \quad (3)$$

$$\Delta B_\theta \equiv B_\theta(R, \theta) - B_\theta(r_c, \theta) \equiv B_0 \epsilon_g \sin \theta, \quad (4)$$

$$\Delta B_\phi \equiv B_\phi(R, \theta) - B_\phi(r_c, \theta) \equiv B_0 \epsilon_s \sin \theta, \quad (5)$$

where $\Delta \alpha$, ϵ_g and ϵ_s depends on the current distribution in the shell region between r_c and R ,

When we regard the crust as an infinitesimally thin layer $\Delta r \rightarrow 0$, ΔB_r vanishes owing to the continuity derived by $\vec{\nabla} \cdot \vec{B} = 0$. However, the discontinuity in tangential components is allowed, and ΔB_θ and ΔB_ϕ may be finite corresponding to the surface current. Three examples of the magnetic field with a discontinuity in the tangential component are shown in Fig. 1. The exterior field is the same for all of them, but $B_\theta(r_c, \theta)$ and $B_\phi(r_c, \theta)$ at the bottom of the crust are different. The current density in the crust may be extremely strong in several cases in the thin limit approximation, and hence the resulting Lorentz force may violate the magnetoelastic equilibrium.

We consider a model for the tangential components of the magnetic field in the crust. The radial functions g' and s in eq. (1) can be approximated using the linear function of $R - r$ within the range $r_c \leq r \leq R$. The radial function g is a quadratic

equation of $R - r$. By using the Ampère–Bio–Savart’s equation $\vec{\nabla} \times \vec{B} = 4\pi\vec{j}/c$, that is matched with eqs. (2)–(5), the radial functions g and s are determined as follows:

$$g = \frac{1}{2}B_0 \left[R^2 + R(R - r) - \left(\frac{1}{2} + \frac{r_c \epsilon_g}{\Delta r} \right) (R - r)^2 \right], \quad (6)$$

$$s = -\frac{B_0 r_c \epsilon_s}{\Delta r} (R - r). \quad (7)$$

The coefficient $\Delta\alpha$ is obtained as:

$$\Delta\alpha = \frac{\Delta r}{r_c} \left[\epsilon_g - 3 - \frac{3\Delta r}{2r_c} \right]. \quad (8)$$

The coefficients ϵ_g and ϵ_s in eqs. (4)–(5) are related to the integration of the electric current in the spherical shell as follows:

$$\frac{4\pi}{c} \int_{r_c}^R r j_\phi dr = B_0 r_c \left(\epsilon_g + \frac{\Delta r}{2r_c} \right) \sin \theta, \quad (9)$$

$$\frac{4\pi}{c} \int_{r_c}^R r j_\theta dr = -B_0 r_c \epsilon_s \sin \theta. \quad (10)$$

For the magnetic field penetrating from inner core to the exterior vacuum, estimating the allowed difference in each magnetic field component is crucial. As shown by eq. (8), $\Delta B_r/B_0$ in the radial component, is of the order $\sim \Delta r/r_c$ and is consistent with the continuity within the limit $\Delta r \rightarrow 0$. However, ΔB_θ and ΔB_ϕ are not simple, and some calculations are necessary. These values were determined by considering the force balance in the crust. Thus ϵ_g and ϵ_s in eqs. (4)–(5), which are related with the surface current in the thin limit, are constrained by the elastic limit of the equilibrium.

2.2 Magnetoelastic equilibrium in crust

The Lorentz force \vec{f} for the dipolar field (1) is expressed as

$$4\pi\vec{f} = \frac{4\pi j_\phi}{cr \sin \theta} \vec{\nabla}(g \sin^2 \theta) - \frac{s}{r^2} \vec{\nabla}(s \sin^2 \theta) + \frac{2}{r^2} (gs' - g's) \sin \theta \cos \theta \vec{e}_\phi, \quad (11)$$

where \vec{e}_ϕ is a unit vector in the ϕ -direction. The acceleration vector due to the Lorentz force is generally decomposed into irrotational and solenoidal components. The irrotational component, which is expressed by the gradient of a scalar function, may be balanced by a change in pressure and gravity. The ratio of the Lorentz force to these dominant forces is typically $(10^{-4} - 10^{-7}) \times (B_0/10^{14} \text{G})^2$ depending on the stellar radius. Therefore, the Lorentz force may be considered as a small perturbation of a spherical stellar structure.

However, there is no solenoidal component of gravity and pressure in barotropic stars. This fact strongly constrains the barotropic equilibrium models. Static or stationary axially symmetric models have been calculated under various conditions using various methods (for example Tomimura & Eriguchi 2005; Yoshida & Eriguchi 2006; Yoshida et al. 2006; Lander & Jones 2009; Duez & Mathis 2010; Fujisawa & Eriguchi 2013; Gourgouliatos et al. 2013; Armaza et al. 2015). The results revealed that the toroidal magnetic field was much smaller than that of the poloidal magnetic field. A similar situation is prevalent for realistic relativistic models (for example Cioffi et al. 2009; Uryū et al. 2019, 2023). The stratified structure of density and pressure, which results in solenoidal acceleration, is a critical factor for stable mixed poloidal and toroidal magnetic fields (for example Reisenegger 2009; Glampedakis et al. 2012; Lander & Jones 2012; Akgün et al. 2013; Yoshida 2019), as reported in an earlier study (Tayler 1980).

In this study, we did not consider stratification; however, the elasticity in the neutron star crust was incorporated. A "curl" of the Lorentz force is balanced with the elastic force \vec{h} . The force balance with the extra force allows different structures, although the elastic force is significantly weaker than the dominant forces and its typical maximum magnitude ratio is 10^{-4} .

A set of approximated equations relevant to magnetoelastic equilibrium is expressed as (Kojima et al. 2021, 2022)

$$(\vec{f} + \vec{h})_\phi = 0, \quad (12)$$

$$[\nabla \times \rho^{-1}(\vec{f} + \vec{h})]_\phi = 0, \quad (13)$$

where ρ denotes the mass density, which is a function of r . We considered only the azimuthal component in eq. (13) because the other poloidal components vanish according to eq. (12) and axial symmetry ($\partial_\phi = 0$).

The i th component h_i is expressed by the shear modulus μ and elastic displacement ξ_i as follows:

$$h_i = \nabla_j (2\mu \sigma_i^j), \quad (14)$$

$$\sigma_{ij} = \frac{1}{2} (\nabla_i \xi_j + \nabla_j \xi_i), \quad (15)$$

where the incompressible motion $\vec{\nabla} \cdot \vec{\xi} = 0$ is assumed in the expression of shear stress tensor σ_{ij} .

The elastic displacement induced by the Lorentz force $\vec{f} = c^{-1} \vec{j} \times \vec{B}$ in eqs. (12)–(13) is expressed by the Legendre polynomials

$P_l(\cos\theta)$ with $l = 2$ only, because the angular dependence of both \vec{j} and \vec{B} is given by $l = 1$ (see eq. (11)). We explicitly write the displacement, which satisfies the incompressible conditions, as follows:

$$\xi_r = \frac{6x_2}{r^2}P_2, \quad \xi_\theta = \frac{x_2'}{r}P_{2,\theta}, \quad \xi_\phi = -rk_2P_{2,\theta}(\theta), \quad (16)$$

where $x_2(r)$ and $k_2(r)$ are the radial functions.

The crust is limited to the inner crust, where the mass density ranges from $\rho_c = 1.4 \times 10^{14} \text{ g cm}^{-3}$ at the core–crust boundary r_c to the neutron drip density, $\rho_1 = 4 \times 10^{11} \text{ g cm}^{-3}$ at R . We ignored the outer crust with extremely small thickness and considered the exterior region as a vacuum. We assumed that the shear modulus is approximately proportional to the mass density such that it depends on the radial coordinate $\mu = \mu(r)$ as follows:

$$\frac{\mu}{\mu_c} = \frac{\rho(r)}{\rho_c} = \left[1 - \left(1 - \left(\frac{\rho_1}{\rho_c} \right)^{1/2} \right) \left(\frac{r - r_c}{\Delta r} \right) \right]^2. \quad (17)$$

where $\mu_c = 10^{30} \text{ erg cm}^{-3}$ is the shear modulus at the core–crust interface (Chamel & Haensel 2008; Lander & Gourgouliatos 2019, for a reasonable approximation).

Using eqs. (6)–(7) eq. (12) is reduced to the following second-order differential equation:

$$(\mu r^4 k_2')' - 4\mu r^2 k_2 + a_2 = 0, \quad (18)$$

where

$$a_2 = \frac{B_0^2}{24\pi} \frac{\epsilon_s r_c}{\Delta r} \left[2R^2 + (R - r)^2 + 2(R - r)^2 \frac{\epsilon_g r_c}{\Delta r} \right]. \quad (19)$$

Equation (13) can be reduced to a fourth-order differential equation as follows:

$$\left[\frac{(\mu y_2)'}{\rho} + 2 \left(\frac{\mu'}{\rho r} \right) x_2' \right]' - \frac{6}{r^2} \left[\frac{\mu y_2}{\rho} + 2 \left(\frac{\mu'}{\rho} \right)' x_2 \right] + b_2 = 0, \quad (20)$$

$$x_2'' - \frac{6}{r^2} x_2 + y_2 = 0, \quad (21)$$

where

$$b_2 = \frac{B_0^2}{24\pi} \left[\left\{ \frac{3R^2 - r^2}{r_c} - \frac{2(R - r)^2}{r_c} \left(\frac{\epsilon_g r_c}{\Delta r} \right) \right\} \left(\frac{1}{\rho r} \right)' \left(\frac{\epsilon_g r_c}{\Delta r} \right) + 4 \left\{ \frac{R - r}{\rho r^2} - (R - r)^2 \left(\frac{1}{\rho r^2} \right)' \right\} \left(\frac{\epsilon_s r_c}{\Delta r} \right)^2 \right]. \quad (22)$$

The source terms a_2 and b_2 in eqs. (19) and (22) are derived from the Lorentz force. Because of the thin shell ($r \approx R$), we neglected the terms proportional to $R - r$ in a_2 and b_2 . Consequently, the dependence of elastic displacement was clear. In case of the axial displacement, $|\xi_\phi| \propto a_2 \propto \epsilon_s$, whereas for polar displacement, $|\xi_p| \propto b_2 \propto \epsilon_g$,

Because the star is assumed to be spherically symmetric, the boundary conditions for eqs. (18), (20), and (21) are given by the force balance across the surfaces at r_c and R . Thus, the shear stress tensors σ_{r_i} ($i = r, \theta, \phi$) vanish because the other stresses of the fluid and magnetic field are assumed to be continuous. The boundary conditions for the radial functions k_2 , x_2 and y_2 at r_c and R are explicitly written as follows:

$$k_2' = 0, \quad (23)$$

$$(r^{-2} x_2)' = 0, \quad (24)$$

$$2rx_2' - 12x_2 + r^2 y_2 = 0. \quad (25)$$

3 NUMERICAL RESULTS

3.1 Spatial shear–distribution

The magnitude of the shear stress is expressed as

$$\frac{1}{2} \sigma_{ij} \sigma^{ij} = (\sigma_{\text{ax}})^2 + (\sigma_{\text{po}})^2, \quad (26)$$

where the total is split to the axial paper σ_{ax} and poloidal part σ_{po} , because they were determined independently. The former is caused by $\xi_\phi \propto \epsilon_s$ and $(\xi_r, \xi_\theta) \propto \epsilon_g$.

Figure 2 illustrates the spatial distribution of σ^2 in a range of $r_c \leq r \leq R$ and $0 \leq \theta \leq \pi$. The profile does not change with the thickness Δr . Fujisawa et al. (2022) calculated σ_{ax} and σ_{po} to obtain a more elaborate current distribution model in the crust. The profiles of σ_{ax} were almost the same. However, the value of σ_{po} slightly differed from that of Fujisawa et al. (2022), which contained two peaks in the radial direction. This complicated structure originates from the electric current distribution adopted in the models.

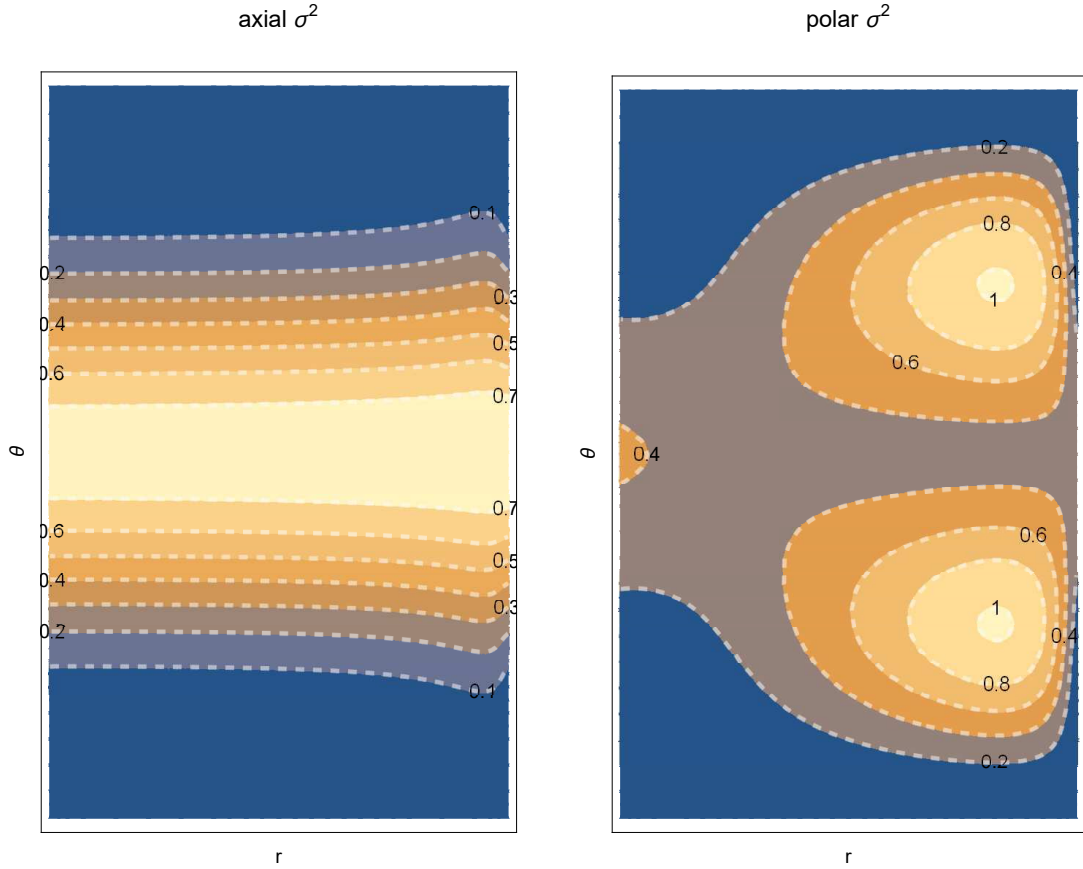


Figure 2. Contour map in $r - \theta$ plane of the magnitude σ^2 normalized by the maximum. The crust region is given by $r_c \leq r \leq R$ and $0 \leq \theta \leq \pi$. The left panel is σ_{ax}^2 for axial displacement, while the right is σ_{pl}^2 for polar displacement.

3.2 Elastic equilibrium range

The elastic equilibrium is possible when the magnitude of the entire crust is less than a threshold value σ_c (the Mises criterion (Malvern 1969; Ushomirsky et al. 2000)), where σ_c is the number $\sigma_c \approx 10^{-2} - 10^{-1}$ (e.g. Horowitz & Kadau 2009; Caplan et al. 2018; Baiko & Chugunov 2018). As both σ_{ax} and σ_{po} depend on the position, the equilibrium conditions are $\sigma_{\text{ax}}^{\text{max}} \leq \sigma_c$ and $\sigma_{\text{po}}^{\text{max}} \leq \sigma_c$. These conditions can be written as follows because $\sigma_{\text{ax}} \propto |\xi_\phi| \propto |\epsilon_s|$ and $\sigma_{\text{po}} \propto |\xi_p| \propto |\epsilon_g|$.

$$|\epsilon_g| \leq \epsilon_g^{\text{max}} \equiv N_* F_g, \quad |\epsilon_s| \leq \epsilon_s^{\text{max}} \equiv N_* F_s, \quad (27)$$

where F_g and F_s are numerically obtained for a model with thickness Δr , and N_* is a dimensionless normalization constant expressed as

$$N_* \equiv \frac{4\pi\mu_c\sigma_c}{B_0^2} \approx 1.3 \times 10^2 \times \left(\frac{\sigma_c}{0.1}\right) \left(\frac{\mu_c}{10^{30}\text{erg cm}^{-3}}\right) \left(\frac{B_0}{10^{14}\text{G}}\right)^{-2}. \quad (28)$$

The numerical results for F_g and F_s are plotted as a function of $\Delta r/r_c$, as shown in Fig. 3. The function F_s was almost proportional to the thickness, whereas F_g changed more significantly with $\Delta r/r_c$. We searched for an empirical fitting curve for these functions. Assuming polynomials, the coefficients were obtained as the best-fit values. The function for the axial part was approximated well by $F_s = \alpha_1 x$, where $x = \Delta r/(0.1r_c)$ and $\alpha_1 = 3.2 \times 10^{-2}$. For the polar part, it was $F_g = \beta_2 x^2 + \beta_4 x^4$, where $\beta_2 \approx 2.0 \times 10^{-2}$, and $\beta_4 \approx 1.8 \times 10^{-2}$.

Our model shows that the upper limits $\epsilon_g^{\text{max}}(\propto F_g)$ and $\epsilon_s^{\text{max}}(\propto F_s)$ approach zero as $\Delta r \rightarrow 0$, although both the electric current and Lorentz force f diverge as $(j, f) \propto (\Delta r)^{-1}$. This convergence to zero results from the severe constraint on the elastic equilibrium. Shear stress σ_{ax} is proportional to $\sigma_{\text{ax}} \propto \xi_\phi \propto \epsilon_s/\Delta r$ and is limited to a finite value σ_c . Therefore, the maximum value of ϵ_s linearly depends on Δr , while the polar component σ_{po} is slightly different. An additional term $[1/(\rho r)]' \sim (\rho_1 R \Delta r)^{-1}$ is involved in the source term; therefore, $\sigma_{\text{po}} \propto \xi_p \propto \epsilon_g/(\Delta r)^2$. The dependence on Δr became quadric, that is, $\epsilon_g \propto (\Delta r)^2$ in the small region Δr .

The change in the tangential component of the magnetic field is formally expressed as eq. (27). However, it is actually less constrained, unless the magnetic field is sufficiently strong, that is, $\sim 10^{14}\text{G}$. For example, for typical pulsars with $B_0 = 10^{12}\text{G}$,

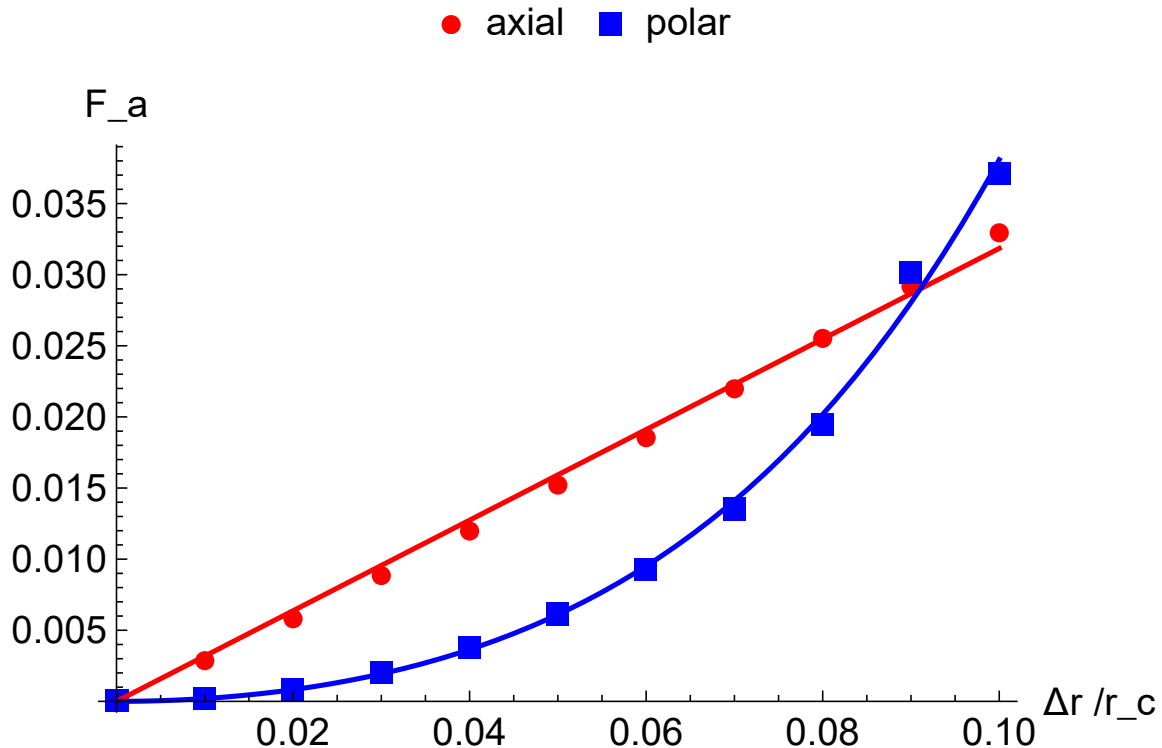


Figure 3. The maximum deviation $F_a = \epsilon_a^{\max} N_*^{-1}$ ($a = s, g$) are plotted as a function of thickness $\Delta r / r_c$. The axial case was approximated by a linear function of $x = \Delta r / (0.1 r_c)$, whereas the polar was approximated by $F_g = \beta_2 x^2 + \beta_4 x^4$.

the condition is $|\Delta B_\theta / B_0| < 10^5$ and $|\Delta B_\phi / B_0| < 10^5$; there is no substantial limit to the tangential components. For example, the direction and magnitude of B_θ at the core-crust interface may completely differ from those at the surface.

However, the magnetoelastic equilibrium range is limited to the strong magnetic-field regime. This constraint is meaningful, because the normalization factor (28) decreases as B_0 increases. $|\Delta B_\theta / B_0| < 1$ and $|\Delta B_\phi / B_0| < 1$ for magnetars with $B_0 > 2.1 \times 10^{14}$ G assuming crustal thickness, $\Delta r / r_c = 0.1$. That is, the tangential components at the core-crust interface are within small extrapolation range from those at the surface. Coefficient $|\epsilon_s|$ represents the ratio of the toroidal to poloidal components at the core-crust interface; $|\epsilon_s| = |\Delta B_\phi / (B_0 \sin \theta)| \approx |B_\phi(r_c, \pi/2) / B_r(r_c, 0)|$. The toroidal component should be smaller than poloidal components for $B_0 > 2.1 \times 10^{14}$ G. The ratio decreases further with an increase in B_0 . Therefore, a strong toroidal component $B_\phi > 10^{15}$ G should be confined to the interior of magnetars $r < r_c$.

4 SUMMARY AND DISCUSSION

We studied the change in the dipolar magnetic field between inner and outer boundaries in neutron star crusts. An arbitrary configuration is allowed under an extremely weak magnetic field. The Lorentz force significantly affects the force balance as the field strength increases. However, even for magnetars with the strongest field strength, the maximum magnitude of the Lorentz force is 10^{-4} times smaller than those of pressure and gravity.

The acceleration resulting from these dominant forces are irrotational in the barotropic case, whereas the Lorentz force generally leads to both irrotational and solenoidal components. Therefore, at the equilibrium, the magnetic field is highly constrained, or a different force exerts a force balance. In this study, we considered that the elastic force was balanced by the solenoidal part of the Lorentz force. The elasticity of the solid crust increases the allowable range of the magnetic field.

The electric current in the thin layer is expressed as using a simple smoothing function determined by the conditions at two surfaces of spherical shells. However, the magnetoelastic force balance is disrupted when the elastic deformation exceeds a certain threshold. The elastic limit based on the Mises criterion constrains the magnetic-field strength.

Our model demonstrates that the difference between magnetic fields in the core crust and on the surface vanishes with decreasing thickness, although the electric current density diverges to the zero limit. The discontinuities of the tangential components are generally allowed as a mathematical boundary condition of the magnetic field across an infinitesimally thin layer; however, the magnetoelastic force balance in the shell with a finite thickness always constrains the change. The allowable range of the magnetic field decreases, although the Lorentz force increases with the decreasing thickness.

For the thickness values of $\Delta r / R \approx 0.02 - 0.1$, which is a realistic range for the crust thicknesses of neutron stars, the change

in the magnetic field was highly constrained in the strong regime $B \sim 10^{14}$ G, where it was difficult for the elastic force to control the Lorentz force. Consequently, the magnetic field at the core–crust interface did not differ significantly from those of the surface owing to its small thickness. The field strength B_ϕ of the toroidal component at the core–crust interface was less than that of the surface dipole field B_0 when $B_0 > 2.1 \times 10^{14}$ G, because the toroidal field is zero in an external vacuum. The strong toroidal component $\sim 10^{16}$ G in the magnetar interior can be inferred from the observed free precession (Makishima et al. 2014, 2016, 2019, 2021a,b); however, the strength should be reduced to $\sim 10^{14}$ G at the bottom of crust. Conversely, a strong component should be confined to the core. Otherwise, an elaborate model would be required. In particular, a superconducting core is crucial. For example, the interior magnetic–field configuration significantly depends on a ratio of the field strength at the crust–core boundary to a characteristic value $H_{c1} \sim 10^{15}$ G for the type-II superconductor (Lander 2013, 2014).

Studies focused on the development of magnetar models are ongoing, and further investigations are required to examine the magnetic deformation of magnetars (for example Frederick et al. 2021; Soldateschi et al. 2021, and references therein), which is relevant to the detection of continuous gravitational waves, and account for the electromagnetic phenomena associated with outbursts (for example Suvorov 2023). The crust has not appropriately been considered in most models. Although the geometry and strength of the internal magnetic fields remain largely unknown, the present results are a step towards gaining insights into the condition at the core–crust interface from the stellar surface.

ACKNOWLEDGMENTS

This work was supported by JSPS KAKENHI Grant Numbers JP19K03850, JP23K03389(YK).

DATA AVAILABILITY

Numerical code and data underlying this article will be shared on reasonable request to the corresponding author.

REFERENCES

- Akgün T., Reisenegger A., Mastrano A., Marchant P., 2013, *MNRAS*, **433**, 2445
 Armaza C., Reisenegger A., Valdivia J. A., 2015, *ApJ*, **802**, 121
 Baiko D. A., Chugunov A. I., 2018, *MNRAS*, **480**, 5511
 Bera P., Jones D. I., Andersson N., 2020, *MNRAS*, **499**, 2636
 Caplan M. E., Schneider A. S., Horowitz C. J., 2018, *Phys. Rev. Lett.*, **121**, 132701
 Chamel N., Haensel P., 2008, *Living Reviews in Relativity*, **11**, 10
 Ciolfi R., Ferrari V., Gualtieri L., Pons J. A., 2009, *MNRAS*, **397**, 913
 Duez V., Mathis S., 2010, *A&A*, **517**, A58
 Duncan R. C., Thompson C., 1992, *ApJ*, **392**, L9
 Frederick S. G., Thompson K. L., Kuchera M. P., 2021, *MNRAS*, **503**, 2764
 Fujisawa K., Eriguchi Y., 2013, *MNRAS*, **432**, 1245
 Fujisawa K., Kisaka S., Kojima Y., 2022, *MNRAS*, **516**, 5196
 Glampedakis K., Andersson N., Lander S. K., 2012, *MNRAS*, **420**, 1263
 Gourgouliatos K. N., Cumming A., Reisenegger A., Armaza C., Lyutikov M., Valdivia J. A., 2013, *MNRAS*, **434**, 2480
 Horowitz C. J., Kadau K., 2009, *Phys. Rev. Lett.*, **102**, 191102
 Kojima Y., 2022, *ApJ*, **938**, 91
 Kojima Y., Kisaka S., Fujisawa K., 2021, *MNRAS*, **506**, 3936
 Kojima Y., Kisaka S., Fujisawa K., 2022, *MNRAS*, **511**, 480
 Kojima Y., Kisaka S., Fujisawa K., 2023, *ApJ*, **946**, 75
 Lander S. K., 2013, *Phys. Rev. Lett.*, **110**, 071101
 Lander S. K., 2014, *MNRAS*, **437**, 424
 Lander S. K., Gourgouliatos K. N., 2019, *MNRAS*, **486**, 4130
 Lander S. K., Jones D. I., 2009, *MNRAS*, **395**, 2162
 Lander S. K., Jones D. I., 2012, *MNRAS*, **424**, 482
 Lander S. K., Andersson N., Antonopoulou D., Watts A. L., 2015, *MNRAS*, **449**, 2047
 Li X., Levin Y., Beloborodov A. M., 2016, *ApJ*, **833**, 189
 Makishima K., Enoto T., Hiraga J. S., Nakano T., Nakazawa K., Sakurai S., Sasano M., Murakami H., 2014, *Phys. Rev. Lett.*, **112**, 171102
 Makishima K., Enoto T., Murakami H., Furuta Y., Nakano T., Sasano M., Nakazawa K., 2016, *PASJ*, **68**, S12
 Makishima K., Murakami H., Enoto T., Nakazawa K., 2019, *PASJ*, **71**, 15
 Makishima K., Enoto T., Yoneda H., Odaka H., 2021a, *MNRAS*, **502**, 2266
 Makishima K., Tamba T., Aizawa Y., Odaka H., Yoneda H., Enoto T., Suzuki H., 2021b, *ApJ*, **923**, 63
 Malvern L. E., 1969, *Introduction to the mechanics of a continuous medium*. Englewood Cliffs, N.J. : Prentice-Hall
 Reisenegger A., 2009, *A&A*, **499**, 557
 Shapiro S. L., Teukolsky S. A., 1983, *Black holes, white dwarfs and neutron stars. The physics of compact objects*. John Wiley & Sons, New York, doi:10.1002/9783527617661

- Soldateschi J., Bucciantini N., Del Zanna L., 2021, *A&A*, **654**, A162
Suvorov A. G., 2023, *MNRAS*, **523**, 4089
Suvorov A. G., Kokkotas K. D., 2019, *MNRAS*, **488**, 5887
Tayler R. J., 1980, *MNRAS*, **191**, 151
Thompson C., Duncan R. C., 1995, *MNRAS*, **275**, 255
Tomimura Y., Eriguchi Y., 2005, *MNRAS*, **359**, 1117
Uryū K., Yoshida S., Gourgoulhon E., Markakis C., Fujisawa K., Tsokaros A., Taniguchi K., Eriguchi Y., 2019, *Phys. Rev. D*, **100**, 123019
Uryū K., Yoshida S., Gourgoulhon E., Markakis C., Fujisawa K., Tsokaros A., Taniguchi K., Zamani M., 2023, *Phys. Rev. D*, **107**, 103016
Ushomirsky G., Cutler C., Bildsten L., 2000, *MNRAS*, **319**, 902
Yoshida S., 2019, *Phys. Rev. D*, **99**, 084034
Yoshida S., Eriguchi Y., 2006, *ApJS*, **164**, 156
Yoshida S., Yoshida S., Eriguchi Y., 2006, *ApJ*, **651**, 462